Results in Physics 61 (2024) 107747

Contents lists available at ScienceDirect

Results in Physics

journal homepage: www.elsevier.com/locate/rinp

DFT+U investigation of electronic, optical, and thermoelectric properties of YAuX (X=Si or Ge or Sn) half-Heusler alloys

Job W. Wafula [a,*], George S. Manyali [b,c], John W. Makokha [a], Yusuf Madallah [b], Soukaina Bouhmaidi [d], Larbi Setti [d]

[a] Department of Science, Technology and Engineering, Kibabii University, 1699, 50200, Bungoma, Kenya
[b] Computational and Theoretical Physics Group (CThePG), Department of Physical Sciences, Kaimosi Friends University, 385, 50309, Kaimosi, Kenya
[c] Physics Department, Masinde Muliro University of Science and Technology, 190, 50100, Kakamega, Kenya
[d] Laboratory of Advanced Science and Technologies, FPL Abdelmalek Essaadi University, Tetouan, Morocco

ARTICLE INFO

Keywords:
PBE+U
Thermoelectric properties
Optical properties
Electronic properties
YAuX (X=si or ge or sn)
DFT

ABSTRACT

Half-heusler alloys are fascinating thermoelectric materials because they have superior mechanical and transport properties. In this study, we used dft+u calculations and the Boltztrap equation to examine the electronic, optical, and thermoelectric properties of YAuSi, YAuGe, and YAuSn half-heusler alloys. The DFT+U approach predicted band gaps of 1.2767 eV, 0.611 eV, and 1.5741 eV for YAuGe, YAUSn, and YAuSi, respectively. We also observed that all materials under consideration have a broad absorption spectrum ranging from 1 eV to 12 eV, with notable peaks in the visible and UV ranges. The obtained opto-electronic properties position the three alloys as promising candidates for photovoltaic applications. Finally, thermoelectric property calculations revealed that the figure of merit values for YAuSi, YAuGe, and YAuSn HH alloys were 0.730, 0.726, and 0.736 at 800 K, respectively suggesting the materials are also suitable candidates for application in the field of thermoelectricity

Introduction

In the aftermath of the global energy crisis, scientists' interest in thermoelectric (TE) materials has expanded significantly in recent years [1–3]. Thermoelectric (TE) materials are capable of recycling a substantial amount of waste heat discarded in applications such as industries and automobile combustion engines in an ecologically friendly and economically beneficial means [4,5]. The conversion efficiency of TE depends on the materials' dimensionless figure of merit zT given by the equation 1;

$$zT = S^2\sigma T/(k_e + k_L) \quad (1)$$

where S, σ, T, k_e, and k_L are the Seebeck coefficient, electrical conductivity, absolute temperature, and electronic and lattice thermal contributions to total thermal conductivity k, respectively [6]. Among the TE material candidates for medium–high temperature applications, PbTe, skutterudites, and half-Heuslers [7] have garnered the greatest attention. However, for large-scale industrial applications, PbTe materials are renowned for their toxic effects and low mechanical strength, whereas skutterudites suffer primarily as a result of their low thermal stability [8]. Fortunately, half-Heusler materials exhibit superior performance ratings making them viable thermoelectric and thermospintronic candidates for medium to high temperature ranges [9–11]. Aside from their great TE performance, their high-quality tensile strength, thermal stability, and low toxicity offers better practical application opportunities [12]. HH compounds have the standard formula ternary intermetallics that is XYZ, in which X is a highly electropositive element, Y is a transition metal featuring the least electro-positive prospective, and Z is a p-block element. HH compounds crystallize in a cubic MgAgAs-type structure with the space group F-43 m, comprised of three interpenetrating ordered fcc sublattices occupied by the X, Y, and Z atoms [13,14]. Since they are known for their semiconducting properties, HH compounds with valence electron count (VEC) of 18 have recently been one of the key research interests, functioning as a system for identifying suitable TE materials. As a result of the closed-shell structure, HH compounds with VEC = 18 are often thermodynamically stable [15]. Over the recent decades, significant progress has been made in improving the TE performance of HH compounds, notably in the 18-electron systems MNiSn, MCoSb, and RFeSb [16]. Intermetallic yttrium compounds are a class of alloys which shows intriguing structural and physical properties [17] hence, the current

* Corresponding author.
E-mail address: jwabwile17@student.kibu.ac.ke (J.W. Wafula).

https://doi.org/10.1016/j.rinp.2024.107747
Received 15 March 2024; Received in revised form 3 May 2024; Accepted 6 May 2024
Available online 11 May 2024

study focused on YAuX (Si or Ge or Sn) alloys. YAuX (Si or Ge or Sn) are among the I-III-IV 18-electron nonmagnetic half-Heusler compounds with energetically preferred configurations when Au element occupies the sublattice C with atomic position; Y(0.50 0.50 0.50), X(0.00 0.00 0.00) and Au(0.25 0.25 0.25) [14]. One of the most important and essential aspects of half-Heusler alloys is that certain physical properties of these alloys are dependent on the quantity of valence electrons [18]. To the best our knowledge the structural, electronic, elastic, optical and thermal properties of the YSiAu, YGeAu and YSnAu half heusler alloys as calculated by GGA-PBE and HSE functionals have been reported in the literature. The literature indicates that the three half-heusler compounds are stable mechanically and dynamically [17,19]. However, the thermoelectric properties of YAuX (Si or Ge or Sn) half heusler alloys are yet to be detailed. Therefore, the current study used the computational techniques to predict the thermoelectric properties using Boltztrap code as well as electronic and optical properties of the three materials from the GGA+U calculations.

Computational details

In this study, the generalized gradient approximation (GGA) with Perdew–Burke–Ernzerhof (PBE) exchange and correlation potentials was utilized [20]. The kinetic energy cut-off for the plane wave function was set to 100 Ry, while the ecutrho cut-off was set to 800 Ry. The Brillouin Zone was sampled with 8 × 8 × 8 using the Monkhorst–Pack grid scheme [21].

When the difference in the total energy of the crystal remained less than 1.0×10^{-5} eV/atom, the self-consistent calculations were judged complete. The geometry was adjusted during the relaxation process until the ionic force was less than 0.03 eV/Å, the maximum ionic displacement was 0.001 Å, and the maximum stress was less than 0.05 GPa. DFT + U calculations were conducted by first introducing a modest Hubbard U value of 0.001 eV to the Au 3d states in YAuGe and YAuSn, as well as the Si 3p states in YAuSi. Initially, a self-consistent field (SCF) computation was carried out, succeeded by an hp.x calculation, resulting in Hubbard U values of 5.0 eV for YAuGe and YAuSn, and 6.0 eV for YAuSi. These Hubbard U values were subsequently applied to the respective states within the three compounds after which the opto-electronic properties were computed. Meanwhile, for temperature-dependent thermoelectric properties, we employed BoltzTraP algorithm as implemented in Quantum ESPRESSO package [22,23]. The relaxation period was regularly set at 10^{-14} s in this context, a number that corresponds to our understanding of the material's behavior which is also equivalent to default value of the code. When calculating the thermoelectric parameters, dense k-points of 40 × 40 × 40 were used. The linearized phonon Boltzmann equation was employed in conjunction with the Phono3py software interfaced to the QE package. A 2 × 2 × 2 supercell was utilized to compute third-order anharmonic and second-order harmonic interatomic force constants. A 9 × 9 × 9 k-point sampling was employed for the former, while a 40 × 40 × 40 k-point sampling was used for the calculation of lattice thermal conductivity.

Results and discussions

Electronic properties

Fig. 2 presents the computed band structures for YGeAu, YSnAu, and YSiAu before and after the incorporation of the Hubbard correction. Among these alloys, YSnAu and YSiAu demonstrate indirect band gaps, while YGeAu functions as a direct band gap semiconductor, as illustrated in Fig. 2 [24,25]. It is also clear from Fig. 1(f) that YSiAu has an inverted band structure which result from Au p levels rising above the s levels [17]. The calculated band gap values for YGeAu, YSnAu, and YSiAu are detailed in Table 1. An analysis of the table reveals that both the hybrid functional (HSE) and the GGA methods have underestimated the band gaps for these materials. However, the GGA+U technique effectively addresses this issue, yielding predicted band gaps of 1.2767 eV, 0.611 eV, and 1.5741 eV for YGeAu, YSnAu, and YSiAu, respectively. These obtained band gap values position the three alloys as promising candidates for photovoltaic applications (see Fig. 1).

Table 1
Calculated band gaps of the three alloys.

Compound	XC	Energy gap (E_g) eV
YGeAu	PBE	–
	HSE06	0.2579
	PBE+U	1.2767
YSiAu	PBE	0.2398
	HSE	0.5366
	PBE+U	1.5741
YSnAu	PBE	0.0332
	HSE	0.2959
	PBE+U	0.611

Optical properties

In this section, we delve into the calculated optical characteristics of the materials. Specifically, we analyze the frequency-dependent real ($\epsilon_1(\omega)$) and imaginary ($\epsilon_2(\omega)$) components of the complex dielectric function. Furthermore, we examine the refractive index $n(\omega)$, extinction coefficient $k(\omega)$, and absorption coefficient $\alpha(\omega)$ of these compounds. The dispersion of the linear optical response for these materials is presented across the optical range spanning from 0 to 20 eV. This provides insight into the response from the static limit to the ultraviolet region of the electromagnetic spectrum. The computation of these optical properties is based on the mathematical relationships outlined in Refs. [26,27] as follows;

$$\alpha(\omega) = \sqrt{2\omega}[(\epsilon_1^2(\omega) + \epsilon_2^2(\omega))^{\frac{1}{2}} - \epsilon_1(\omega)]^{\frac{1}{2}} \tag{2}$$

$$n(\omega) = \frac{1}{2}[(\epsilon_1^2(\omega) + \epsilon_2^2(\omega))^{\frac{1}{2}} + \epsilon_1(\omega)]^{\frac{1}{2}} \tag{3}$$

$$L\omega = \frac{\epsilon_1(\omega)}{\epsilon_1^2(\omega) + \epsilon_2^2(\omega)} \tag{4}$$

$$R(\omega) = \frac{(n-1)^2 + k^2}{(n+1)^2 + k^2} \tag{5}$$

$$k(\omega) = \frac{1}{\sqrt{2}}[(\epsilon_1^2(\omega) + \epsilon_2^2(\omega))^{\frac{1}{2}} - \epsilon_1(\omega)]^{\frac{1}{2}} \tag{6}$$

With $\epsilon_2(\omega)$ representing the imaginary part of the dielectric function and $\epsilon_1(\omega)$ denoting the real part of the dielectric function, Fig. 2 illustrates a graphical representation of the studied optical properties. At $\omega = 0$, the computed values for $\epsilon_1(\omega)$ are 9.9290 (PBE calculation) and 4.2496 (PBE+U calculation) for YGeAu. In the case of YSnAu, the static limit value is 10.1738 and 8.6560 before and after applying the Hubbard U value, respectively. For YSiAu, the $\epsilon_1(\omega)$ value at 0 frequency is 9.4394 and 4.4455 before and after applying the Hubbard U value.

The ϵ_1 curve reveals two distinct regions: one characterized by sharp peaks depicting various electronic transitions. The peaks reach a maximum intensity of 14.335, corresponding to an energy of 1.780 eV for YGeAu before applying the Hubbard U and 6.6466 at an energy of 4.9439 eV after applying the Hubbard U value. For YSnAu, the maximum peaks before applying the Hubbard U value occur at an intensity of 14.7395 at an energy of 1.6975 eV and 12.5765 at an energy of 1.6652 eV. In the case of YSiAu, the maximum peak's intensity is 15.7404 at an energy of 1.9934 eV before applying the Hubbard U, and 6.1102 at an energy of 5.6613 eV after applying the Hubbard U value. Another region exhibits an exponential decrease in

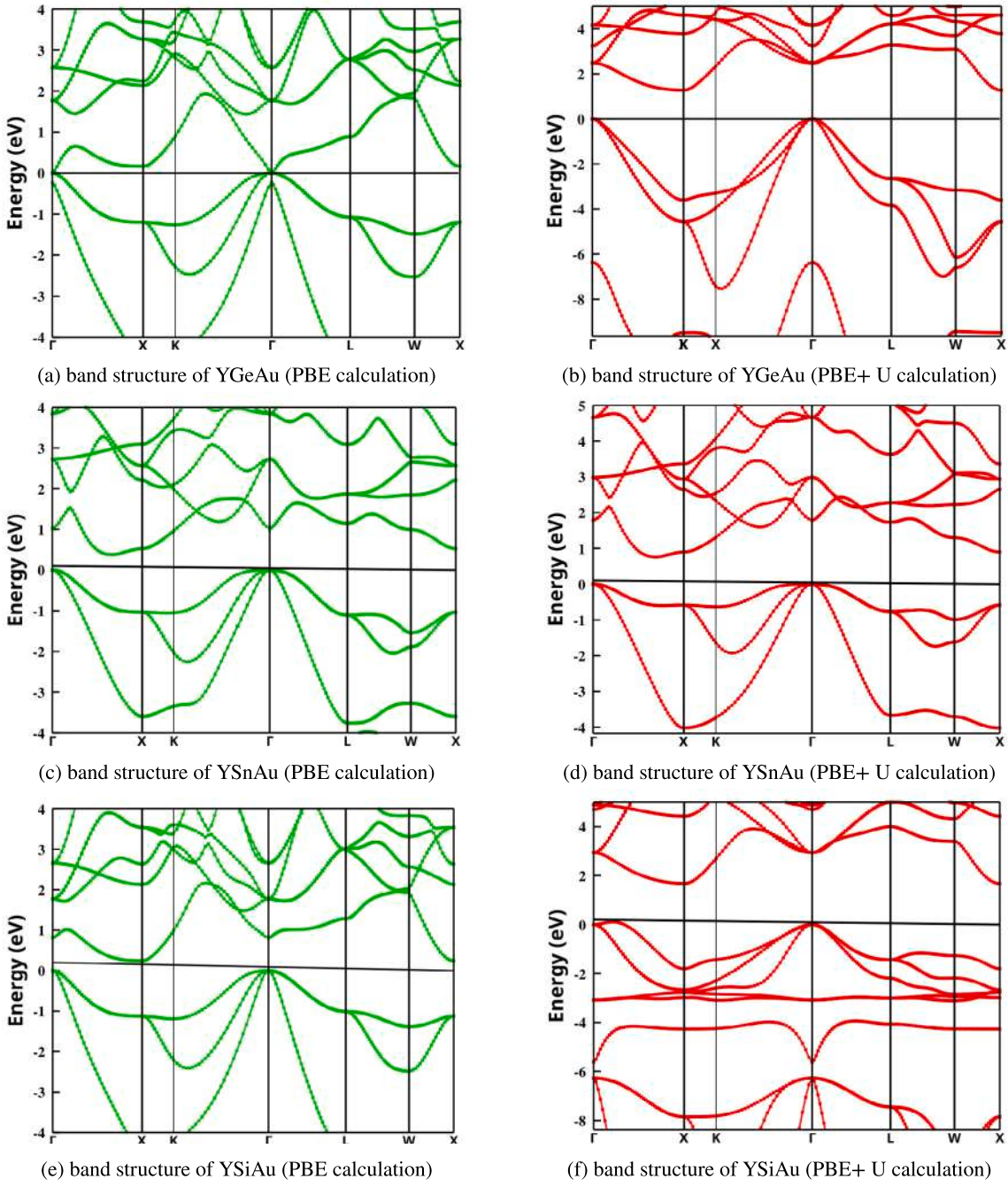

(a) band structure of YGeAu (PBE calculation)

(b) band structure of YGeAu (PBE+ U calculation)

(c) band structure of YSnAu (PBE calculation)

(d) band structure of YSnAu (PBE+ U calculation)

(e) band structure of YSiAu (PBE calculation)

(f) band structure of YSiAu (PBE+ U calculation)

Fig. 1. Electronic band structures of YGeAu, YSnAu and YSiAu respectively as calculated by DFT and DFT+U.

the variation of $\epsilon_1(\omega)$, reaching a minimum value before the peaks become less pronounced and eventually cancel out. Examining the imaginary part of the dielectric function ($\epsilon_2(\omega)$) within the range of 0 eV to 12 eV reveals prominent peaks. The maximum peak values for YGeAu are 15.3978 and 5.9975 before and after the application of Hubbard U, respectively. For YSnAu, the values before and after applying Hubbard U are 15.1040 and 13.5563, respectively. In the case of YSiAu, the obtained values are 16.6707 without Hubbard U and 5.5079 with the inclusion of Hubbard U. Following this region, there is a subsequent region where $\epsilon_2(\omega)$ rapidly approaches 0. Refractive index of covalent compounds typically exhibit higher values compared to ionic compounds. This discrepancy arises from the fewer number of electrons shared by ions in ionic compounds in comparison to covalent compounds. Additionally, in ionic compounds, there is a lesser distribution of electrons throughout the structure, and the interaction with incident photons tends to decelerate these electrons. The corresponding values of the refractive index $n(0)$ at zero frequency for YGeAu were recorded as 2.0137 and 3.1517 with and without the Hubbard U value, respectively. For YSnAu, the values were 3.0171 and 3.8004 with and without Hubbard U values, respectively. In the case of YSiAu, the static refractive index values were obtained as 3.0538 before the application of Hubbard U and 2.0747 after the application of Hubbard U. It is noteworthy that the static limit refractive index values conform to the relationship $n_0 = \sqrt{\epsilon_1(0)}$.

All materials exhibit a broad absorption spectrum spanning from 1 eV to 12 eV, with significant peaks occurring within the visible and UV regions. This observation suggests that these materials could be well-suited for opto-electronic applications. In Fig. 2(e), the dispersion relation for the extinction coefficient $k(\omega)$ is presented. The modulation

of the extinction coefficient follows a similar pattern to that of the imaginary part of the dielectric function, given their direct relationship.

Upon examining the reflectivity plots, it is apparent that the majority of peaks are situated between 4 eV and 10 eV, although their values are less than 1. This region is followed by a sharp decrease in reflectivity as photon energy increases. Another property investigated is energy loss, providing insight into how energy is dissipated by fast electrons entering a medium. The majority of energy loss peaks occur at higher energies, around 8 eV, which is outside the ultraviolet–visible light (UV–V) region. Importantly, no sharp energy loss peaks were observed within the visible light region. This observation suggests that the materials are well-suited for photovoltaic applications.

In the reflectivity curve (part (f) of Fig. 2), it is evident that both compounds exhibit low reflectivity within the visible light and ultraviolet region, with maximum peaks occurring at intensities of 0.89 for YGeAu, 0.94 for YSnAu, and 0.85 for YSiAu. These reflectivity values are smaller compared to those of absorption.

Thermo-electric properties

Assuming the relaxation time constant, the Boltztrap package (based on semi-classical theory) is used to calculate the temperature-dependent TE parameters. Low thermal conductivity and resistivity values are essential for good thermo-electric materials, paired with high Seebeck coefficient (S) values. The calculated TE parameters plotted against temperature (0–800 K) which is approximately within the recently theoretical predicated melting points of the materials [19] as implemented in Boltztrap code are shown in Fig. 3(a–d).

Electrical conductivity (σ)

Fig. 3(a) depicts the electrical conductivity of YAuX (Si or Ge or Sn) HH alloys over the relaxation time constant/τ $(\Omega\ m\ s)^{-1}$. The electrical conductivity quantifies the quantity of electrons/holes in the conduction band [28]. It is also a measure of the flow of electronic charge in a substance [29]. At 50 K, YAuSi, YAuGe and YAuSn HH alloys have the electrical conductivity values of 7.789×10^{17} $(\Omega\ m\ s)^{-1}$, 8.641×10^{17} $(\Omega\ m\ s)^{-1}$ and 5.020×10^{17} $(\Omega\ m\ s)^{-1}$ respectively. On the other hand, the electrical conductivity values of 8.946×10^{18} $(\Omega\ m\ s)^{-1}$, 8.396×10^{18} $(\Omega\ m\ s)^{-1}$ and 8.713×10^{18} $(\Omega\ m\ s)^{-1}$ for YAuSi, YAuGe and YAuSn HH alloy respectively were detected at higher temperature of 800 K. It is clear from Fig. 3(a) that electrical conductivity increases exponentially from low to high temperature. This indicates that electrical conductivity is modest at low temperatures but large at high temperatures due to the fact that, at high temperatures bond breaking produces a large number of electrons with high kinetic energy. This findings validates the variation of electrical conductivity of semiconductor as a function of temperature. We noted that YAuSi HH alloy is thus an excellent semiconductor at temperatures above 500 K since it liberates more electrons than the other two HH alloys. However, YAuGe showed better electrical conductivity at low temperature below 300 K.

Thermal conductivity

Thermal conductivity can be calculated as $\kappa = \kappa_e + \kappa_l$, where κ_e and κ_l stand for electronic and lattice thermal conductivity respectively [30]. Because the lattice vibration is outside the range of the Boltztrap algorithm, only the electronic mode of thermal conductivity over the relaxation time constant κ_e/τ is estimated, as illustrated in Fig. 3(b). The Wiedemann–Franz law describes the relationship between electronic thermal conductivity (e) and electrical conductivity (κ_e) using the equation below:

$$k_e = L\sigma T \tag{7}$$

In the free electron model, the Lorentz number (L) is given as 2.45×10^{-8} V K^{-2}. Fig. 3(b) demonstrates that thermal conductivity increases linearly with temperature over the range studied. As temperatures rise, electrons get thermally stimulated, resulting in increased heat [31,32]. It has been noticed that all materials exhibit almost identical behavior. The electronic contribution to thermal conductivity κ begins low and increases with temperature. κ values of YAuSi, YAuGe and YAuSn HH alloys are 4.79×10^{14} W/K m s, 4.45×10^{14} W/K m s and 4.72×10^{14} W/K m s at 50 K respectively and 1.37×10^{12} W/K m s, 1.37×10^{12} W/K m s and 1.37×10^{12} W/K m s at 800 K respectively. Furthermore, as shown in Fig. 3(b), all of the materials display exponential development in thermal conductivity as temperature rises from 50 K to 800 K since electrons are stimulated by increased heat.

Lattice thermal conductivity (K_l)

Fig. 3(e) shows a plot of the obtained lattice thermal conductivity as a function of temperature. The lattice thermal conductivity of YAuSi, YAuSn and YAuGe HH alloys at 300 K are; 0.07, 0.10 and 0.01 W m^{-1} K^{-1} respectively. Additionally, it is observed that the lattice thermal conductivity diminishes with rising temperatures. Fig. 4 illustrates the variation of phonon lifetime with frequency. It is evident from the figure that the phonon lifetime of YAuSn is shorter compared to YAuGe and YAuSi. This observation suggests that YAuSn possesses lower group velocity, smaller mean free path (MFP), and shorter phonon lifetime.

Seebeck coefficient (S)

The Seebeck coefficient and electrical conductivity, as measured by the power factor (PF) plays crucial role in determining the thermo-electric efficiency of semiconductors [32]. In the study the Seebeck coefficient values of YAuSi, YAuGe and YAuSn half-heusler alloys were calculated as a function temperature as indicated in Fig. 3(c). At 50 K, the YAuSi, YAuGe and YAuSn half-heusler alloys registered the S values of 125.15 μV/K, 115.90 μV/K and 154.99 μV/K respectively while 221.11 μV/K, 219.38 μV/K and 223.21 μV/K at 800 K. From Fig. 3(c) we also noted that the Seebeck coefficients of the three alloys increase with temperature up to 500 K however beyond 500 K the S values remain almost constant and this is attributed to atomic bond disruption. YAuSn alloy has best thermoelectric properties since the S values are slightly higher than that of YAuGe and YAuSn. Furthermore, all the alloys in this study have positive S value which clearly demonstrates that the materials are p-type semiconductor, thus holes are the dominating charge carriers.

Figure of merit (zT)

The figure of merit (zT) was predicted as a function of temperature and details provided in Fig. 3(d). The figure of merit for YAuSi, YAuGe and YAuSn HH alloys at 800 K are 0.730, 0.726 and 0.736, respectively. YAuSn HH alloy, exhibiting a notably high Seebeck value at 800 K, demonstrates a commendable figure of merit of 0.736 at the same temperature, surpassing the other two HH alloys. We observed that figure of merit increase with rise in temperature however, the zT almost remains constant beyond 500 K. At low temperatures, the prevalence of phonon scattering takes precedence, causing a decline in thermal conductivity (κ). Consequently, this phenomenon can yield an elevation in ZT. During intermediate temperatures, the electrical conductivity (σ) frequently experiences enhancement owing to heightened carrier concentration or mobility, thereby potentially resulting in an elevated ZT. Conversely, at high temperatures, thermal conductivity (κ) typically escalates due to amplified phonon transport, while electrical conductivity may reach a plateau or decline due to increased scattering. This scenario often leads to a reduction in ZT. When zT equals or exceeds unity, the material is considered a promising thermo-electric material [33].

Conclusion

In this study, we successful calculated the electronic and thermo-electric properties of YAuSi, YAuGe and YAuSn HH alloys using DFT+U

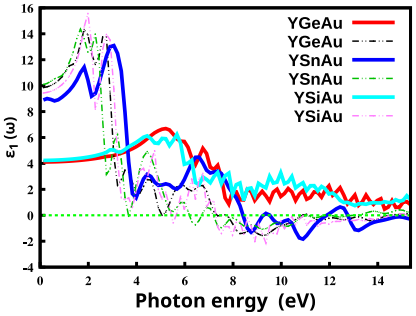

(a) Real part of the dielectric ($\epsilon_1(\omega)$) function as a function of photon energy

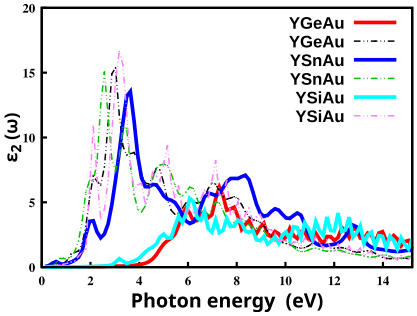

(b) Imaginary part of the dielectric ($\epsilon_2(\omega)$)function as a function of photon energy)

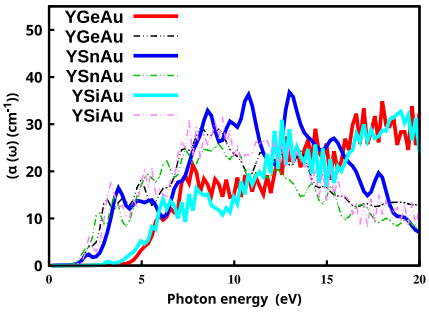

(c) Absorption coefficient ($\alpha(\omega)$) as a function of photon energy

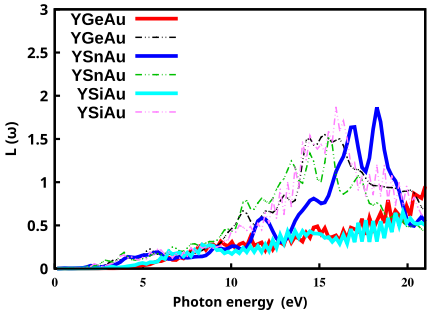

(d) Energyloss ($L(\omega)$) curves as a function of photon energy

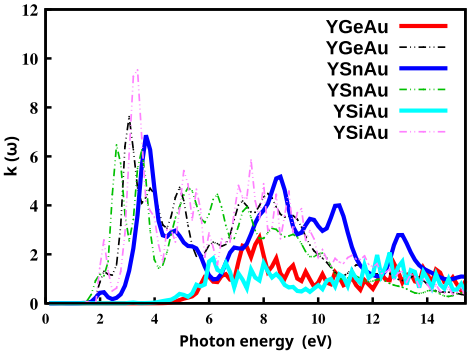

(e) Extinction coefficients ($k(\omega)$) as a function of photon energy

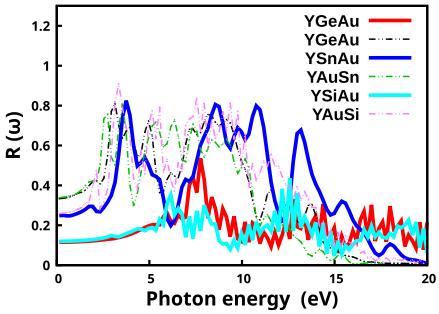

(f) Reflectivity ($R(\omega)$) as a function of photon energy

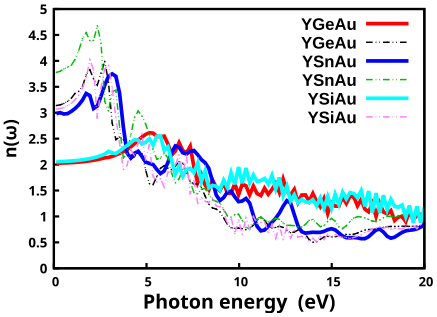

(g) Refractive index ($n(\omega)$) as a function of photon energy

Fig. 2. Optical properties of YGeAu, YSnAu and YSiAu; the dotted lines represents PBE calculation while the complete lines are for DFT+U calculation.

and BoltzTrap code. DFT+U method was found to predict better band structure diagrams which agree well with other theoretical studies. The opto-electronic properties obtained indicate that the three alloys hold promise as potential candidates for photovoltaic applications. Furthermore, calculations of their thermoelectric properties disclosed figure of merit values of 0.730, 0.726, and 0.736 at 800 K for the YAuSi, YAuGe, and YAuSn HH alloys, respectively, further indicating their suitability for utilization in the realm of thermoelectricity.

CRediT authorship contribution statement

Job W. Wafula: Writing – review & editing, Writing – original draft, Software, Methodology, Investigation, Formal analysis, Data curation, Conceptualization. **George S. Manyali:** Writing – review & editing, Supervision, Software, Methodology, Investigation, Formal analysis, Data curation. **John W. Makokha:** Writing – review & editing, Supervision, Software, Resources, Formal analysis. **Yusuf Madallah:** Writing

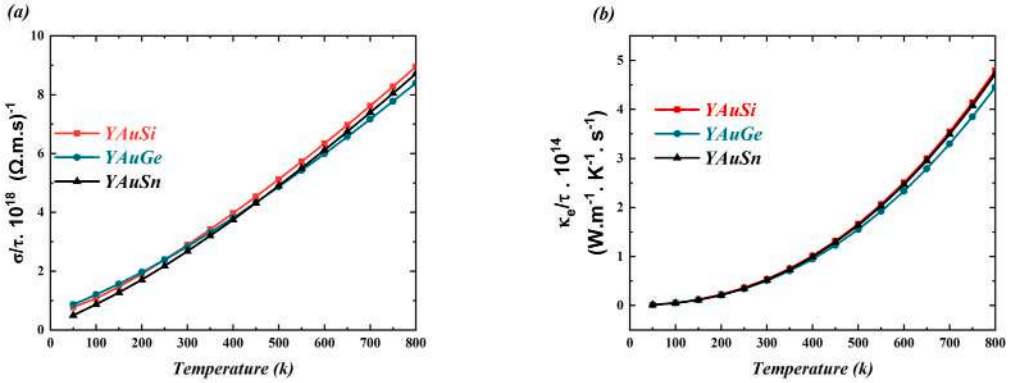

(a) Electrical conductivity (σ) of YAuSi, YAuGe and YAuSn alloys (b) Thermal conductivity (κ) of YAuSi, YAuGe and YAuSn alloys

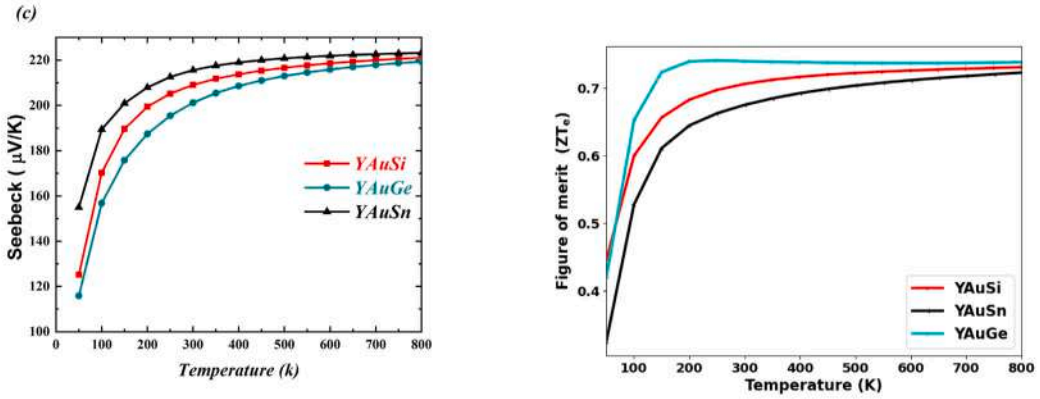

(c) Seebeck coefficients of YAuSi, YAuGe and YAuSn alloys (d) Figure of merit (zT) of YAuSi, YAuGe and YAuSn alloys

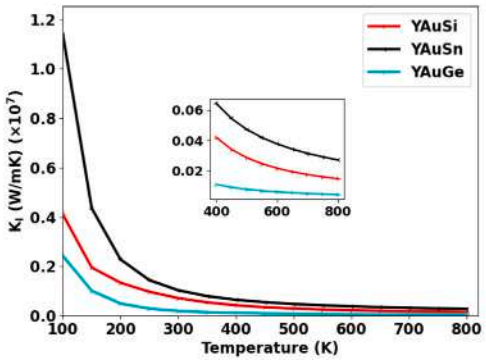

(e) Lattice thermal conductivity of YAuSi, YAuGe and YAuSn alloys.The inset shows Lattice thermal conductivity when temperature goes from 400 K up to 800 K

Fig. 3. Temperature dependent thermo-electric properties of YGeAu, YSnAu and YSiAu HH alloys.

– review & editing, Writing – original draft, Software, Methodology, Investigation, Formal analysis. **Soukaina Bouhmaidi:** Writing – review & editing, Software, Methodology, Investigation, Data curation. **Larbi Setti:** Writing – review & editing, Supervision, Resources, Methodology, Investigation.

Declaration of competing interest

The authors declare that they have no known competing financial interests or personal relationships that could have appeared to influence the work reported in this paper.

Data availability

Data will be made available on request.

Acknowledgments

The authors acknowledges centre for high performance computing based in South Africa for provision of the computation resource. Secondly, the authors appreciates Professor Larbi Setti who offered the workstation for the calculations, which was instrumental in obtaining the thermo-electric data.

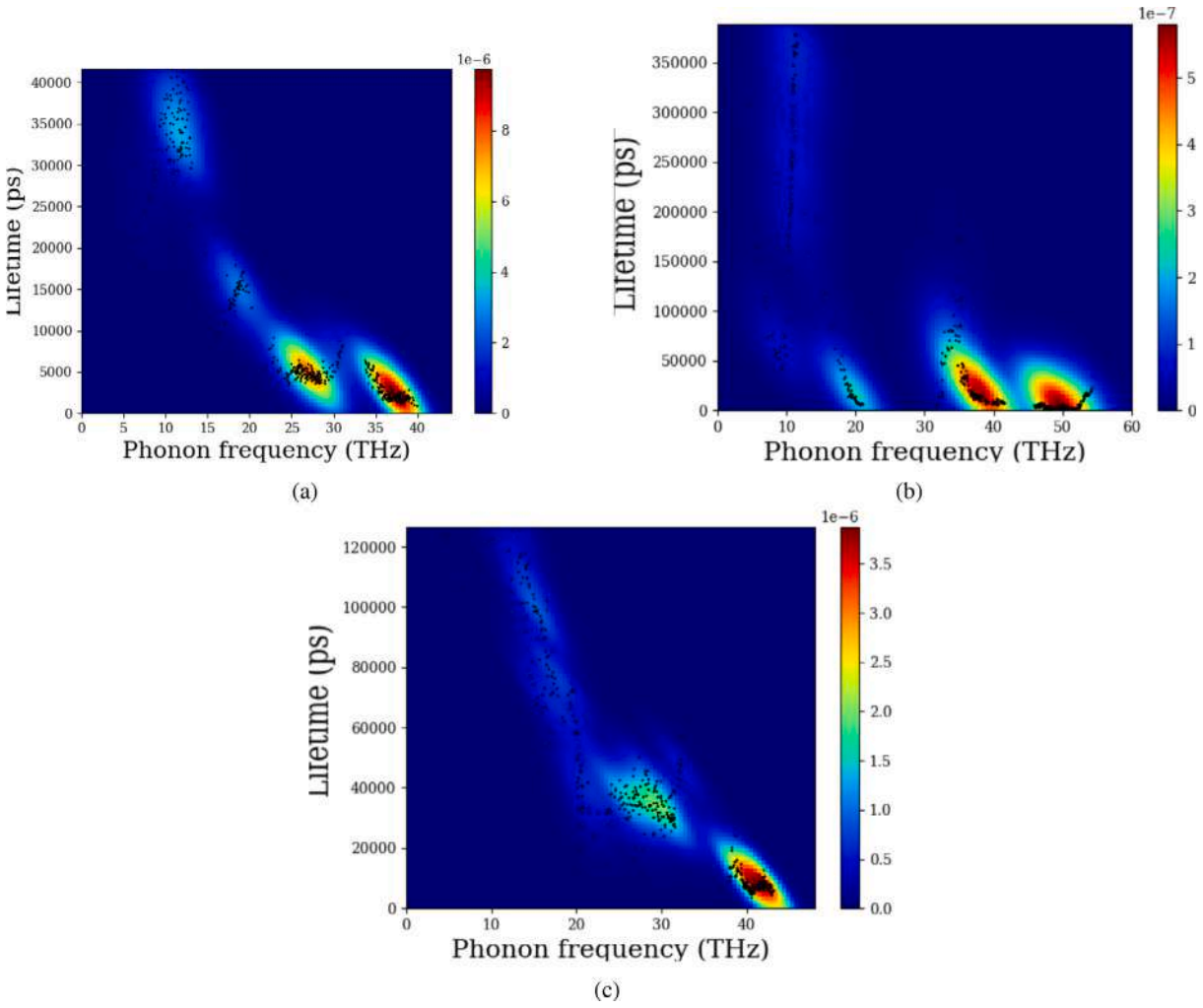

Fig. 4. Phonon lifetime in pico-second as a function of phonon frequency in Tera-Hertz in (a) YAuGe (b) YAuSi and (c) YAuSn HH alloys. Phonon modes are displayed in black, while the colored background represents the density of the phonon modes in the corresponding region.

References

[1] Abubakr M, Abbas Z, Naz A, Khalil H, Khan MA, Kim H, Khan K, Ouladsmane M, Rehman S, Kim D-k, et al. First principles quantum analysis of structural, electronic, optical and thermoelectric properties of XCu2GeQ4 (X=Ba, Sr and Q=S, Se) for energy applications. Opt Quantum Electron 2023;55(10):1–21.

[2] Rached Y, Caid M, Merabet M, Benalia S, Rached H, Djoudi L, Mokhtari M, Rached D. A comprehensive computational investigations on the physical properties of TiXSb (X: Ru, Pt) half-Heusler alloys and Ti2RuPtSb2 double half-Heusler. Int J Quantum Chem 2022;122(9):e26875.

[3] Diaf M, Righi H, Rached H, Rached D, Beddiaf R. Ab initio study of the properties of Ti2PdFe (Ru) Sb2 double half-heusler semiconducting alloys. J Electron Mater 2023;52(10):6514–29.

[4] Huang L, Zhang Q, Yuan B, Lai X, Yan X, Ren Z. Recent progress in half-Heusler thermoelectric materials. Mater Res Bull 2016;76:107–12.

[5] Mehtougui N, Bendahma F, Rached Y, Mana M, Rached D, Caid M, Boukortt A, Ghalem Y. Novel semiconductor compounds XZrZ (X=Ni, Cu and Z=C, B) suitable for clean energy in optoelectronic and thermoelectric devices. Comput Condens Matter 2022;32:e00730.

[6] Snyder GJ, Toberer ES. Complex thermoelectric materials. Nat Mater 2008;7(2):105–14.

[7] Caballero-Calero O, Ares JR, Martín-González M. Environmentally friendly thermoelectric materials: High performance from inorganic components with low toxicity and abundance in the earth. Adv Sustain Syst 2021;5(11):2100095.

[8] Pei Y, Shi X, LaLonde A, Wang H, Chen L, Snyder GJ. Convergence of electronic bands for high performance bulk thermoelectrics. Nature 2011;473(7345):66–9.

[9] Zhu T, Fu C, Xie H, Liu Y, Zhao X. High efficiency half-Heusler thermoelectric materials for energy harvesting. Adv Energy Mater 2015;5(19):1500588.

[10] Rached Y, Caid M, Rached H, Merabet M, Benalia S, Al-Qaisi S, Djoudi L, Rached D. Theoretical insight into the stability, magneto-electronic and thermoelectric properties of XCrSb (X: Fe, Ni) half-Heusler alloys and their superlattices. J Supercond Nov Magn 2022;35(3):875–87.

[11] Rached D, Boumia L, Caid M, Rached Y, Ait Belkacem A, Rached H, Merabet M, Benalia S. The half-metallic ferromagnetic and thermoelectric responses of the potential thermo-spintronic compounds CrTiRhZ (Z: Al or Si) QHA. Indian J Phys 2023;1–10.

[12] Yu J, Xing Y, Hu C, Huang Z, Qiu Q, Wang C, Xia K, Wang Z, Bai S, Zhao X, et al. Half-heusler thermoelectric module with high conversion efficiency and high power density. Adv Energy Mater 2020;10(25):2000888.

[13] Graf T, Felser C, Parkin SS. Simple rules for the understanding of Heusler compounds. Prog Solid State Chem 2011;39(1):1–50.

[14] Gruhn T. Comparative ab initio study of half-Heusler compounds for optoelectronic applications. Phys Rev B 2010;82(12):125210.

[15] Xia K, Hu C, Fu C, Zhao X, Zhu T. Half-Heusler thermoelectric materials. Appl Phys Lett 2021;118(14).

[16] Yu J, Xia K, Zhao X, Zhu T. High performance p-type half-Heusler thermoelectric materials. J Phys D: Appl Phys 2018;51(11):113001.

[17] Lekhal A, Benkhelifa F, Mecabih S, Abbar B, Bouhafs B. Structural and electronic properties of non-magnetic intermetallic YAuX (X=Ge and Si) in hexagonal and cubic phases. Bull Mater Sci 2016;39:195–200.

[18] Erden Gulebaglan S, Kilit Dogan E. A comparison study of the structural electronic, elastic and lattice dynamic properties of ZrInAu and ZrSnPt. Z Natforsch A 2021;76(6):559–67.

[19] Wafula JW. Structural, elastic, electronic, optical and thermal properties of YMAu (M=Si or Ge or Sn) Half-Heusler compounds; A DFT study. Results Mater 2023;100413.

[20] Perdew JP, Burke K, Ernzerhof M. Generalized gradient approximation made simple. Phys Rev Lett 1996;77(18):3865.

[21] Monkhorst HJ, Pack JD. Special points for Brillouin-zone integrations. Phys Rev B 1976;13(12):5188.

[22] Madsen GK, Carrete J, Verstraete MJ. BoltzTraP2, a program for interpolating band structures and calculating semi-classical transport coefficients. Comput Phys Comm 2018;231:140–5.

[23] Giannozzi P, Andreussi O, Brumme T, Bunau O, Nardelli MB, Calandra M, Car R, Cavazzoni C, Ceresoli D, Cococcioni M, et al. Advanced capabilities for materials modelling with Quantum ESPRESSO. J Phys: Condens Matter 2017;29(46):465901.

[24] Youcef A, Bettahar N, Cheref O, Eddine S, Rached D, Benkhettou N, Bezzerga D, et al. Topologically nontrivial phase in Na2CuX (X=As, Sb, Sn and Bi) full Heusler compounds: Insights from DFT-based computer simulation. Rev Mex Fís 2023;69(2 Mar-Apr):020501.

[25] Boughena A, Benalia S, Cheref O, Bettahar N, Rached D. A first-principles investigation of band inversion in topologically nontrivial Na2AgX (X=As, Sb and Bi) full Heusler compounds. 2021, arXiv preprint arXiv:2106.13184.

[26] Yusuf M, Saouma FO, Manyali GS, Wafula JW, Pembere A. First principles study of thermo-physical and opto-electronic properties of NaCuTe, NaCuSe and NaScSn as potential photovoltaics. Physica B 2024;415954.

[27] Yusuf M, Saouma FO, Manyali GS, Wafula JW, Huxley O. DFT investigation of structural, elastic, electronic, thermodynamic and optical properties of KCuZ (Z=Te, Se) solar absorbers. Solid State Commun 2023;370:115219.

[28] Mahmood Q, Ghrib T, Rached A, Laref A, Kamran M. Probing of mechanical, optical and thermoelectric characteristics of double perovskites Cs2GeCl/Br6 by DFT method. Mater Sci Semicond Process 2020;112:105009.

[29] Berri S. Thermoelectric properties of A2BCl6: a first principles study. J Phys Chem Solids 2022;170:110940.

[30] Asghar M, Zanib M, Khan MA, Niaz S, Noor N, Dahshan A. Tuning of the bandgap of Rb2ScAgX6 (X=Cl, Br, I) double perovskites through halide ion replacement for solar cell applications. Mater Sci Semicond Process 2022;148:106819.

[31] Moço D, Malta JF, Santos LF, Lopes EB, Gonçalves AP. Thermoelectric properties of nickel and selenium co-doped tetrahedrite. Materials 2023;16(3):898.

[32] Bouhmaidi S, Uddin MB, Pingak RK, Ahmad S, Rubel MHK, Hakamy A, Setti L. Investigation of heavy thallium perovskites TlGeX3 (X=Cl, Br and I) for optoelectronic and thermoelectric applications: A DFT study. Mater Today Commun 2023;37:107025.

[33] Haque E, Hossain MA. Origin of ultra-low lattice thermal conductivity in Cs2BiAgX6 (X=Cl, Br) and its impact on thermoelectric performance. J Alloys Compd 2018;748:63–72.